

**Wiley Analytical Science**

# **Wiley Analytical Science Virtual Conference**

**November 9-17**

**For the 3rd time, The Wiley Analytical Science  
Conference is back!**

**It's all happening November 9 - 17**

The Wiley Analytical Science Virtual Conference will bring together thousands of researchers and practitioners to share current developments in science and industry. Join for exciting presentations from experts in the fields of analytical and bioanalytical chemistry, pharmaceutical research, materials science, lab automation, and related disciplines.

Register to learn about recent developments & applications in:

- Microscopy
- Spectroscopy
- Mass Spectrometry
- Separation Science
- Much more!

**Register here**

**WILEY**

## Electrically Tunable and Dramatically Enhanced Valley-Polarized Emission of Monolayer WS<sub>2</sub> at Room Temperature with Plasmonic Archimedes Spiral Nanostructures

Wei-Hsiang Lin\*, Pin Chieh Wu, Hamidreza Akbari, George. R. Rossman, Nai-Chang Yeh\* and Harry A. Atwater\*

Wei-Hsiang Lin, Hamidreza Akbari, Prof. Harry A. Atwater

Department of Applied Physics, California Institute of Technology, Pasadena, CA 91125, USA

E-mail: [haa@caltech.edu](mailto:haa@caltech.edu) and [whlin@alumni.caltech.edu](mailto:whlin@alumni.caltech.edu)

Prof. Pin Chieh Wu

Department of Photonics, National Cheng Kung University, Tainan 70101, Taiwan

Prof. George. R. Rossman

Department of Geological and Planetary Sciences, California Institute of Technology, Pasadena, CA 91125, USA

Prof. Nai-Chang Yeh

Department of Physics, California Institute of Technology, Pasadena, CA 91125, USA

E-mail: [ncyeh@caltech.edu](mailto:ncyeh@caltech.edu)

Keywords: transition metal dichalcogenides, exciton-plasmon interaction, valleytronics, circular dichroism, chiral plasmonic metasurface

### Abstract

Monolayer transition metal dichalcogenides (TMDs) have intrinsic valley degrees of freedom, making them appealing for exploiting valleytronic applications in information storage and processing. WS<sub>2</sub> monolayer possesses two inequivalent valleys in the Brillouin zone, each valley coupling selectively with a circular polarization of light. The degree of valley polarization (DVP) under the excitation of circularly polarized light (CPL) is a parameter that determines the purity of valley polarized photoluminescence (PL) of monolayer WS<sub>2</sub>. Here, we report efficient tailoring of valley-polarized PL from monolayer WS<sub>2</sub> at room temperature (RT) through surface plasmon-exciton interactions with plasmonic Archimedes spiral (PAS) nanostructures. The DVP of WS<sub>2</sub> at RT can be enhanced from < 5% to 40% and 50% by using 2 turns (2T) and 4 turns (4T) of PAS, respectively. Further enhancement and control of excitonic valley polarization is demonstrated by electrostatically doping monolayer WS<sub>2</sub>. For CPL on WS<sub>2</sub>-2TPAS heterostructures, the 40% valley polarization is enhanced to 70% by modulating the carrier doping via a backgate, which may be attributed to the screening of momentum-dependent long-range electron-hole exchange interactions. The manifestation of electrical tunability in the valley-polarized emission from WS<sub>2</sub>-PAS heterostructures presents a new strategy towards harnessing valley excitons for application in ultrathin valleytronic devices.

This article has been accepted for publication and undergone full peer review but has not been through the copyediting, typesetting, pagination and proofreading process, which may lead to differences between this version and the [Version of Record](#). Please cite this article as [doi: 10.1002/adma.202104863](https://doi.org/10.1002/adma.202104863).

This article is protected by copyright. All rights reserved.

## Introduction

Monolayer 2H-phase transition metal dichalcogenides (TMDs)  $\text{MX}_2$  are direct band gap semiconductors that consist of an atomic layer of transition metal atoms (M) sandwiched between a top and a bottom layer of halogen atoms (X) that are arranged in their respective hexagonal lattice structure.<sup>[1,2]</sup> The band structures of monolayer TMDs<sup>[3-7]</sup> consist of two inequivalent K ( $-K$ ) valleys in the hexagonal Brillouin zone. The strong spin-orbit coupling and broken inversion symmetry in monolayer 2H-TMDs result in a large energy splitting between the top spin-up (spin-down) and bottom spin-down (spin-up) valence bands in the K ( $-K$ ) valley.<sup>[8-13]</sup> This spin-valley coupling gives rise to valley-dependent optical selection rules:<sup>[14-16]</sup> Circularly polarized light with positive helicity ( $\sigma^+$ ) couples to the K valley and that of the negative helicity ( $\sigma^-$ ) couples to the  $-K$  valley. It is therefore possible to selectively populate and manipulate the different valleys (K or  $-K$ ) by means of circularly polarized light (CPL).<sup>[11,15]</sup> The spin and valley degrees of freedom (DOF) in these monolayer TMDs materials provide an important platform for exploring new condensed matter physics and for applications in spintronic and valleytronic devices. Noting that the control of circularly polarized emission of light is also a key step towards developing functional optical devices for applications in display technologies<sup>[17,18]</sup> and quantum information processing/communication,<sup>[19-21]</sup> manipulation of the valley DOF is one of the promising approaches to achieving practical information processing devices that are more energy efficient than existing charge-based technologies.

Although accessing different valley DOF through CPL has been demonstrated in several TMDs, including molybdenum disulfide ( $\text{MoS}_2$ ),<sup>[8-10]</sup> molybdenum diselenide ( $\text{MoSe}_2$ ),<sup>[22]</sup> tungsten disulfide ( $\text{WS}_2$ ),<sup>[13,23]</sup> and tungsten diselenide ( $\text{WSe}_2$ ),<sup>[24-27]</sup> it has been challenging to manipulate the valley polarization and the resulting photoluminescence (PL) of monolayer 2H-TMDs at room temperature (RT) because of the weak light-matter interaction and substantial defects<sup>[13]</sup> in these atomically thin

This article is protected by copyright. All rights reserved.

layers. Various approaches, such as applying an in-plan electric field,<sup>[24,28]</sup> an out-of-plan magnetic field,<sup>[29–33]</sup> or a localized magnetic field,<sup>[34]</sup> have been proposed in an attempt to enhance the circular dichroism (CD) of PL in these TMDs.

An alternative approach to enhancing the CD of PL in TMDs is by means of chiral plasmonic metasurfaces.<sup>[34–43]</sup> This approach is based on the strong optical chirality in metallic chiral metasurfaces and the enhancement of light-matter interaction through localized surface plasmon resonance (LSPR) modes. Specifically, the confined LSPR modes can strongly interact with the carriers within the monolayer TMD material to form a compact, functional nanophotonic devices. Furthermore, the geometry-dependent LSPR modes of chiral plasmonic metasurface provide wavelength tunability for the wide emission range of different TMDs. Thus, implementing chiral plasmonic metasurfaces<sup>[44–54]</sup> on 2H-TMDs is likely an efficient approach to manipulating the CD of PL in these monolayer materials.

In this study, a metal-dielectric-metal (MDM) structure that consists of monolayer  $WS_2$  and plasmonic Archimedes spiral ( $WS_2$ -PAS) nanostructures is designed to investigate the monolayer  $WS_2$  exciton-plasmon interaction and to manipulate the valley-polarized PL in  $WS_2$ -PAS heterostructures by spectroscopic measurements and numerical simulations. The device configuration included a monolayer  $WS_2$  single crystal grown by chemical vapor deposition (CVD) and transferred to a substrate of 60 nm-thick  $SiO_2$  on top of a 150 nm-thick gold reflection layer. A 60 nm-thick gold film was subsequently deposited on the  $WS_2/SiO_2/Au$  structure, and then either righthanded (RH) or lefthanded (LH) spiral gold rings were patterned on the gold film by E-beam lithography. To demonstrate the crystallinity of our monolayer  $WS_2$  samples, we performed Raman spectroscopic studies of the  $A_{1g}$  and  $E_{2g}^1$  modes using a 514.3 nm laser (2.41 eV) as the excitation source. Additionally, X-ray photoelectron spectroscopy (XPS) was conducted to examine the chemical

composition and valence states of monolayer WS<sub>2</sub>, as detailed previously.<sup>[13]</sup> Representative Raman and XPS characterization results of a monolayer WS<sub>2</sub> are given in Figures S1 and S2, respectively.

The magnitude of the degree of valley polarization (DVP) in as-grown monolayer WS<sub>2</sub> was < 5 % at RT, whereas those of the DVP in monolayer WS<sub>2</sub>-2TRHPAS (with 2 turns of PAS) and WS<sub>2</sub>-4TRHPAS (with 4 turns of PAS) under the excitation of right-handed circularly polarized (RCP) light were found to be 40% and 50%, respectively. Here the DVP value ( $P_{\text{DVP}}$ ) is defined by the following expression:

$$P_{\text{DVP}} = \frac{I(\sigma^+) - I(\sigma^-)}{I(\sigma^+) + I(\sigma^-)}, \quad (1)$$

where  $I(\sigma^+)$  and  $I(\sigma^-)$  denote the right- and left-handed circular polarization-resolved PL intensity, respectively. In contrast, the corresponding values of the DVP under the excitation of left-handed circularly polarized (LCP) light decreased to  $\sim 5\%$  in both monolayer WS<sub>2</sub>-2TRHPAS and WS<sub>2</sub>-4TRHPAS heterostructures. Additionally, the DVP values could be further enhanced by applying a back-gated voltage  $V_{\text{Gate}}$  from 40% for  $V_{\text{Gate}} = 0$  up to 70% for  $V_{\text{Gate}} = -20$  V. This finding suggests that modulating the carrier doping level can enhance the valley polarization by screening the long-range electron-hole exchange interactions, thus reducing the momentum-dependent inter-valley scattering. The capability of enhancing and tuning the degrees of valley polarization in monolayer 2H-TMDs at room temperature by plasmonic chiral metasurfaces and electrical gating offers new opportunities towards developing valley-dependent optoelectronic devices for energy-efficient information processing.

Our proposed underlying mechanism for tailoring the valley-polarized PL of monolayer 2H-WS<sub>2</sub> by PAS and gated voltage is schematically shown in Figures 1a-1c: In WS<sub>2</sub> monolayer, excitons in the K valley couple with the right handed (RH) circularly polarized light ( $\sigma^+$ ), whereas excitons in the  $-K$  valley couple with the left handed (LH) circularly polarized light ( $\sigma^-$ ). However, after  $\sigma^+$  light excitation, the exciton population pumped in the K valley could be scattered to the  $-K$  valley due to

phonon- and defect-induced inter-valley scattering. Therefore, the DVP of PL was usually low at RT as shown in Figure 1a. On the other hand, when WS<sub>2</sub> monolayer interacts with the RHPAS structures in the near-field range, optical absorption is enhanced, which contributes to more  $\sigma^+$  excitons under right handed CPL in the WS<sub>2</sub>-RHPAS structure. In the K valley, the  $\sigma^+$  excitons interact with the right handed (RH) chiral near-field of the surface plasmon polaritons (SPP) of PAS, leading to giant optical activities that contribute to enhanced the PL intensity in the far field, as shown in Figure 1b. In contrast, the  $\sigma^-$  exciton emission generated from  $-K$  valley is suppressed by the interaction with the RH chiral near-field. The interplay of exciton generation, exciton emission, and inter-valley scattering in each valley contributes to far-field measurements of the valley-polarized PL spectra. As schematically shown in Figure 1a, the DVP of the PL emission depends on the decay rates of the excitons at K ( $\gamma_K$ ) valley,  $-K$  valley ( $\gamma_{-K}$ ), and the inter-valley scattering rate between the two valleys. Therefore, the DVP can be enhanced through increasing the decay rates of the valley-polarized excitons or decreasing the inter-valley scattering rate in two valleys by the chiral Purcell effect. Although the presence of RHPAS structures contributes to increasing the decay rate of the  $\sigma^+$  excitons, the inter-valley scattering is still significant so that the DVP enhancement is limited. The latter situation may be mitigated by applying a gate voltage between the WS<sub>2</sub> and the gold mirror, as shown in Figure 1c, so that the excess carrier doping helps screen the momentum-dependent long-range electron-hole exchange interaction, thereby reducing the inter-valley scattering and leading to significantly enhanced DVP in gated WS<sub>2</sub>-RHPAS heterostructures.

## Results and Discussion

Coupling TMDs with chiral plasmonic metasurfaces can enhance the light-matter interaction through the confined localized surface plasmon and can be a promising approach to enhance the CD of PL in 2H-TMDs. Figure 2a is a schematic illustration of the metal-dielectric-metal (MDM) structure that consists of a monolayer WS<sub>2</sub> and plasmonic Archimedes spiral nanostructures (WS<sub>2</sub>-PAS) under

the excitation of CPL. The WS<sub>2</sub> monolayer was grown by chemical vapor deposition (CVD) method and then transferred onto a substrate consisting of a 60 nm-thick SiO<sub>2</sub> layer on top of a 150 nm-thick gold mirror layer. The Archimedes spiral rings were patterned by E-beam lithography on a 50 nm-thick Au film deposited on the top of the WS<sub>2</sub> monolayer.

Figure 2b shows the PL intensity differences between the as-grown monolayer WS<sub>2</sub> and the MDM structure of a monolayer WS<sub>2</sub> integrated with right-handed plasmonic Archimedes spiral (RHPAS) nanostructures. Under the excitation of right-hand circularly polarized light (RCP, red), the PL intensity of the WS<sub>2</sub>-2TPAS heterostructure was enhanced by more than 10 times relative to that of the as-grown WS<sub>2</sub> (green). In contrast, the PL intensity was barely enhanced under the excitation of left-handed circularly polarized light (LCP, blue). The strong polarization contrast is a good indicator for exciton-plasmon coupling, and the quantitative strength can be characterized by the intensity enhancement factor (EF). The enhancement factor (EF) is defined as  $EF = I_{wi}/I_{wo}$ , where  $I_{wi}$  ( $I_{wo}$ ) is the maximum intensity of WS<sub>2</sub> with (without) the Archimedes spiral nanostructures. Figure 2b shows the EF is larger than 10 between the RCP emission of the WS<sub>2</sub>-2TPAS and that of the as-grown WS<sub>2</sub>, whereas the EF is nearly 1 between the LCP emission of the WS<sub>2</sub>-2TPAS and that of the as-grown WS<sub>2</sub>. This spectroscopic phenomenon suggests that coupling WS<sub>2</sub> with PAS nanostructures is an efficient way for tailoring the exciton-plasmon interaction through actively controlling the polarization of the incident light. The inset of Figure 2b is a scanning electron microscope (SEM) image of arrays of WS<sub>2</sub>-2TPAS heterostructure, where the scale bar represents 5 μm.

To understand the enhancement of PL intensity and valley polarization, we note that in the saturation regime, the EF consists of contributions from three processes: an enhanced absorption rate ( $\alpha$ ), an enhanced light extraction factor ( $\epsilon$ ), and a total rate enhancement factor ( $\gamma_{on}/\gamma_{off}$ ) from the Purcell effect that includes both radiative and nonradiative rates as well as metallic losses. Thus, we have  $EF = \alpha\epsilon(\gamma_{on}/\gamma_{off})$ , where  $\gamma_{on}$  is the total decay rate of WS<sub>2</sub> coupled to the PAS

nanostructures, and  $\gamma_{\text{off}}$  is the total decay rate of the as-grown  $\text{WS}_2$ . The total rate enhancement factor can be directly determined by the time-resolved PL measurements. As shown in Figure S3, the extracted decay time of the as-grown  $\text{WS}_2$  was 1.5 ns ( $\tau_{\text{off}} = 1/\gamma_{\text{off}}$ ), whereas that for the  $\text{WS}_2$ -2TPAS was 0.3 ns ( $\tau_{\text{on}} = 1/\gamma_{\text{on}}$ ). The  $\text{WS}_2$ -2TPAS heterostructures displayed a significantly faster decay rate and the total rate enhancement was found to be  $(\gamma_{\text{on}}/\gamma_{\text{off}}) \sim 5$  ( $\sim 500\%$ ). Therefore, the underlying Purcell factor ( $F_p$ ) could be estimated from the relation  $F_p = \left( \frac{F_p \gamma_R}{F_p \gamma_R + \gamma_M} \right) \left( \frac{\gamma_{\text{on}}}{\gamma_{\text{off}}} - 1 \right) \eta_{\text{off}}^{-1}$ , as detailed in Supporting Information S2. Here  $\gamma_R$  and  $\gamma_M$  are the radiative and metallic-loss decay rates, respectively, and  $\eta_{\text{off}} \equiv \gamma_R / (\gamma_R + \gamma_{NR})$  represents the quantum efficiency of the as-grown  $\text{WS}_2$ . From the measured value  $(\gamma_{\text{on}}/\gamma_{\text{off}}) \sim 5$  and using  $\left( \frac{F_p \gamma_R}{F_p \gamma_R + \gamma_M} \right) \approx 1$  in the limit of a large  $F_p$  and taking  $\eta_{\text{off}} = 0.1$ ,<sup>[24–27]</sup> we obtained an underlying Purcell factor  $F_p \approx 40$ . The coupling factor  $\beta \equiv F_p / (1 + F_p)$  thus estimated was around 98%, which implied that nearly all the PL emission was coupled to the MDM nano-cavity mode.

The exciton-plasmon interaction in  $\text{WS}_2$ -PAS nanostructures is dependent on the incident laser power, the PL intensity of as-grown  $\text{WS}_2$ , and the specific designs of the Archimedes spiral nanostructures. The laser power dependence of PL, under 514 nm RCP laser excitation in  $\text{WS}_2$ -2TPAS with RH spiral nanostructures, was revealed in Figure 2c. The PL intensity of the  $\text{WS}_2$ -2TRHPAS was found to increase rapidly with the laser power from 1.9  $\mu\text{W}$  to 16.2  $\mu\text{W}$ , and the PL peak position also exhibited a slight blue shift with increasing laser power up to 5.5  $\mu\text{W}$ , and then remained invariant from 5.5  $\mu\text{W}$  to 16.2  $\mu\text{W}$ . Figure 2d presented a log-log plot of the power-dependent PL intensity of  $\text{WS}_2$  with (red, triangle) and without (blue, inversed triangle) the plasmonic coupling effect. The relationship between PL intensity ( $I_{\text{PL}}$ ) and laser power ( $P_{\text{laser}}$ ) could be approximately expressed by the relation  $I_{\text{PL}} = (P_{\text{laser}})^m$ , where  $m$  denoted a constant. For both  $\text{WS}_2$  with and without spiral structures, the corresponding  $m$  values were fitted to be  $\sim 1.37$  for laser powers ranging from 1.9  $\mu\text{W}$  to 16.2  $\mu\text{W}$ , and a maximum enhancement factor  $\varepsilon$  reached  $> 10$  at 9.1  $\mu\text{W}$ .

This article is protected by copyright. All rights reserved.

Valley polarization in monolayer TMDs could be induced by CPL excitations and detected by PL measurements at room temperature. Figure 3 shows the comparison of the valley polarized PL spectra between an as-grown monolayer WS<sub>2</sub> and a WS<sub>2</sub>-2TRHPAS heterostructure under the excitations of RCP and LCP light. The wavelength of the excitation laser was 514 nm ( $E_{\text{pump}} = 2.41$  eV), which was far away the neutral exciton resonant energy ( $E_x = 2$  eV). A linear polarizer and a quarter-wave plate (400-800 nm) were placed after the laser to obtain circularly polarized light. The polarized PL signal was resolved by a broadband polarizer and a quarter-wave plate placed before the spectrometer.

The representative PL spectra of the as-grown WS<sub>2</sub> single crystal exhibited similar behavior under both the RCP and LCP excitations, as shown in Figures 3a and 3d. The obtained DVP (< 5%) was consistent with previous studies at room temperature. According to the valley-dependent optical selection rule of TMDs,  $\sigma^+$  ( $\sigma^-$ ) excitations only coupled to the specific excitonic transitions in the K (-K) valley so that the corresponding light emission should have carried single handedness. However, as schematically shown in Figure 1, when the K valley was selectively excited by  $\sigma^+$  polarized light, the PL emission contained not only  $\sigma^+$  signals from polarized excitonic transitions in the K valley but also  $\sigma^-$  signals from the -K-valley, which may be primarily attributed to optical phonon-assisted intervalley scattering of excitons from K to -K-valley, with spin angular momentum exchanged at a finite rate.

As shown in Figure 3b, the PL intensity of the  $\sigma^+$  emission spectra from the WS<sub>2</sub>-RHPAS heterostructure was significantly enhanced relative to that of the  $\sigma^-$  emission spectra under the  $\sigma^+$  excitation. In contrast, the PL intensity of the  $\sigma^+$  and  $\sigma^-$  emission spectra from the WS<sub>2</sub>-2TRHPAS heterostructure did not exhibit any enhancement under the  $\sigma^-$  excitation, as shown in Figure 3e. For comparison between the DVP under  $\sigma^+$  and  $\sigma^-$  excitations, the corresponding DVP spectra are shown in Figures 3c and 3f for the as-grown WS<sub>2</sub> and the WS<sub>2</sub>-2TRHPAS heterostructure, respectively. We find that the value of DVP from the WS<sub>2</sub>-2TRHPAS heterostructure increased by ~

55% under the  $\sigma^+$  excitation and decreased by  $\sim 1\%$  under the  $\sigma^-$  excitation. These notable DVP values of the WS<sub>2</sub>-2TRHPAS may be attributed to the nontrivial interaction between the excitons in WS<sub>2</sub> and the chiral plasmonic mode in the PAS.

To better understand the exciton-plasmon interactions, we further investigated the effect of different plasmonic structures on the valley-polarized PL spectra. Figure S4a show the SEM image of 2-turn RHPAS, and the structural parameters of the PAS are given in Figure S4b . The spiral structure has an inner radius  $r_0 = 200$  nm, width = 50 nm, and pitch = 310 nm so that the outer radius  $r = r_0 + N(R_{\text{plasmon}}/2)$ , where  $N$  is the integer number of turns and  $R_{\text{plasmon}} = 620$  nm is the resonance wavelength of the surface plasmon polariton, which coincides with the neutral A-exciton emission wavelength in the PL spectrum of monolayer WS<sub>2</sub>. These structure parameters were chosen by the COMSOL simulation results (Figures S4 and S5) so that strong field enhancement could be achieved at the ring center under the RCP excitation. Moreover, the pitch of the spiral must match the wavelength of the surface plasmon polariton (SPP). Overall, proper choices of the structural parameters are essential to optimize the exciton-plasmon interaction in the PAS structures.

Figure S4c shows the near-field PL intensity in the x-y plane under RCP excitation. When a 2-turn RHPAS interacted with the RCP light, the surface plasmon polaritons (SPPs) were generated by the RH spiral structures and coherently propagated toward to the ring center to form a constructive focus point. The excitons thus generated (RCP emission) interacted constructively with the SPP field, which resulted in enhanced PL intensity at the center of the RH spiral structure. Figure S4e shows the corresponding phase map of the 2-turn RHPAS in the x-y plane under RCP excitations. The phase at the center of the spiral ring revealed a locally uniform phase distribution as shown by the white dotted circle in Figure S4e. Thus, the constructive interaction of excitons and SPP fields resulted in significant PL enhancement under the RCP excitation. In contrast, the LCP excitation induced weak E-field distribution without focusing effects, as shown in Figure S4d. At the center of the spiral ring the phase varied from  $-\pi$  to  $\pi$  as shown in Figure S4f. The SPPs propagated as before with the LCP

This article is protected by copyright. All rights reserved.

excitation, but the phase could not compensate to yield constructive, focusing effects at the center of the spiral structure.

Interestingly, the E-field and phase distribution were also dependent on the number of turns of the PAS, and the dependence of the exciton-plasmon interaction on the number of turns is manifested in Figure 4 and Figure S5. In Figure 4a-4d, we show the SEM images of 1-, 2-, 3- and 4-turn PAS arrays on a monolayer  $WS_2$  single crystal. The corresponding PL intensity maps under RCP excitation are shown in Figure 4e-4h, where it is evident that the PL intensity became dramatically enhanced when the  $WS_2$  monolayer coupled with the 2-turn and 4-turn RH spiral rings. In contrast, the intensity enhancement almost disappeared in the case of 1-turn and 3-turn RH spiral rings. The corresponding E-field distributions are shown in Figures S5a-S5d, where we found that the focusing effects only happened for the RHPAS structures with an even number of turns. This finding may be explained in terms of the phase compensation effects induced by the outer and inner spiral coupling at subwavelengths. The phase distribution of the PAS heterostructure demonstrated a strong dependence on the number of turns in the spiral structure, as shown in Figure S5e-S5h. For PAS with an even number of turns, the phase at the center of the spiral ring revealed a locally uniform phase distribution, as manifested by the white dotted circle Figure S5f and S5h. In contrast, the phase changed from  $-\pi$  to  $\pi$  for PAS with an odd number of turns.

In addition to the PL intensity, spatially resolved DVP maps further revealed that the DVP was also dependent on the number of turns in the PAS structure, as shown in Figures 4i-4l and Figures S6-S9 for 1-, 2-, 3- and 4-turn PAS arrays on a monolayer  $WS_2$ . For a RHPAS with an odd number of turns, the DVP values were lower than 10%. In contrast, for a RHPAS with an even number of turns, the DVP values were much enhanced, ranging from 35% to 55% for 2T-RHPAS and from 40% to 55% for 4T-RHPAS. Such strongly enhanced valley polarization associated with the far-field PL mapping of

the WS<sub>2</sub>-PAS heterostructure may be attributed to the consequences of the near-field interaction between the valley excitons in WS<sub>2</sub> and the surface plasmon modes in the PAS.

We further investigated the effect of the PAS resonance wavelength ( $R_{\text{plasmon}}$ ) on the enhancement of the DVP by performing PL measurements on WS<sub>2</sub>-2TRHPAS heterostructures with three different resonance wavelengths  $R_{\text{plasmon}} = 310$  nm ( $2.42 \times 10^{14}$  Hz), 620 nm ( $4.84 \times 10^{14}$  Hz) and 930 nm ( $7.26 \times 10^{14}$  Hz), and the corresponding PL spectra and the DVP values are shown in Figure S10. These results revealed the best room temperature DVP enhancement occurred at  $R_{\text{plasmon}} = 620$  nm, which coincided with the neutral A-exciton emission wavelength.

Neutral excitons are the natural low-energy excitations of a charge-neutral semiconductor, whereas trions are only formed in the presence of excess charge. Therefore, the intensity of trion emissions is generally dependent on the amount of excess charge in the semiconductor. For this reason, trion emissions were usually not found in the PL spectra of our CVD-grown monolayer WS<sub>2</sub> samples unless a back gate voltage was applied. For the gated samples, the PL spectra typically exhibited additional emissions at 30–60 meV below the neutral excitonic line, which may be attributed to the emission from negatively charged trions ( $X^-$ ). Thus, by simply varying the applied back gate voltage, we were able to control the ratio between neutral exciton and charged trion emissions.

Figure 5a shows a schematic of a back-gated FET device based on WS<sub>2</sub>-2TRHPAS and an SEM image of the top view of such a device. For a given gate voltage, there were two well-defined PL spectral components associated with the emission bands of the neutral excitons (X) and the negatively charged trions ( $X^-$ ). We found that the emission near 620 nm (2 eV) from neutral excitons (X) was dominant around the charge neutrality point at  $V_{\text{Gate}} = 0$ . The optimal line shape fitting for the spectral contributions was found to be a mixed Gaussian–Lorentzian function, as shown in Supporting Information Figure S11 for WS<sub>2</sub> and Figure S12 for WS<sub>2</sub>-2TRHPAS, respectively. The PL

spectral evolution of these two emission bands with the gate voltage is illustrated in Figures S13 and S14 for as-grown 1L-WS<sub>2</sub>, and in Figures 5b-5c for WS<sub>2</sub>-2TRHPAS. We note that the trion-to-exciton intensity ratios of both WS<sub>2</sub>-2TRHPAS and 1L-WS<sub>2</sub> exhibited similar dependence on the gate voltage, as shown in Figure 5c and Figure S13c, respectively.

Figure S13a shows a color map of the PL spectra from a back-gated field effect device of as-grown 1L-WS<sub>2</sub> with the back-gate voltages ( $V_{\text{Gate}}$ ) from  $-25$  to  $25$  V at RT. For negative gate voltages ( $V_{\text{Gate}} < 0$ ), both X and X<sup>-</sup> features were visible, and the integrated intensity of the X-peak gradually decreased while that of the X<sup>-</sup>-peak increase when  $|V_{\text{Gate}}|$  decreases. In contrast, for positive gate voltage ( $V_{\text{Gate}} > 0$ ), the integrated intensity of the X-peak gradually decreased and the X<sup>-</sup>-peak became dominant with increasing  $V_{\text{Gate}}$  due to electrostatic doping, which led to a single X<sup>-</sup>-peak profile for sufficiently high carrier densities, implying that the Fermi level moved much closer to the energy of the bound trion states than to that of the neutral exciton states.

Helicity resolved PL spectra of an as-grown gated WS<sub>2</sub> sample are shown in Figures S14b and S14c for  $V_{\text{Gate}} = -2$  V and  $+5$  V, respectively. When the WS<sub>2</sub> sample was negatively gated at  $V_{\text{Gate}} = -2$  V, both X and X<sup>-</sup> emissions revealed relatively low DVP of 4.2% and 5.8%, respectively. Similarly, at a positive gate voltage ( $V_{\text{Gate}} = 5$  V), both X and X<sup>-</sup> emissions also revealed low DVP of 4.7% and 5.1%, respectively. These low DVP values implied that the significant inter-valley scattering was insensitive to the gate voltage in the as-grown WS<sub>2</sub> sample.

In contrast to the small effect of the gate voltage on the DVP of the as-grown WS<sub>2</sub> sample, the gate voltage dependent DVP became significantly different in the case of 1L-WS<sub>2</sub>-2TRHPAS heterostructures. Figure 5b-5c show the PL spectral evolution of X and X<sup>-</sup> emissions from the 1L-WS<sub>2</sub>-2TRHPAS sample with the gate voltage. Additionally, polarization-resolved PL spectra of the 1L-WS<sub>2</sub>-2TRHPAS sample under  $\sigma^+$  excitations are shown in Figures 5d-f for  $V_{\text{Gate}} = 0$ ,  $-10$  V and  $-20$  V, respectively. For  $V_{\text{Gate}} = 0$ , the photon-excited excitons at the K valley were more populated under

$\sigma^+$  excitations, which corresponded to the valley-polarized state in pristine WS<sub>2</sub> and WS<sub>2</sub>-2TRHPAS. By increasing the electron density via decreasing the gate voltage from 0 to -10 V and -20 V, the difference between the  $\sigma^+$  and  $\sigma^-$  components of the PL spectra became more significant, implying increased valley polarization of the neutral excitons. Specifically, we found that the values of DVP for  $V_{\text{Gate}} = 0, -10 \text{ V}$  and  $-20 \text{ V}$  were 40%, 50% and 70%, respectively, suggesting significantly enhanced valley polarization as the applied bias was detuned from the charge neutral point. The corresponding RT spatially resolved DVP map and PL maps of a WS<sub>2</sub>-2TRHPAS device at  $V_{\text{Gate}} = -20 \text{ V}$  are shown in Figures 5g and Figure S15, respectively.

To gain further insights into this behavior, we performed gate-dependent transport measurements, using a scheme where a positive bias induced hole-doping and a negative bias introduced electron-doping. We observed typical n-type transport behavior with on/off current ratios greater than  $10^4$  at room temperature, as shown in Figure S16. The doped carrier density  $n$  under gate voltage  $V_{\text{Gate}}$  was estimated from the geometric capacitance and back-gate voltage using the following relation

$$n = (\epsilon\epsilon_0/t_{\text{ox}})(V_{\text{Gate}} - V_{\text{CNP}})/e, \quad (2)$$

where  $\epsilon = 3.9$  is the dielectric constant of SiO<sub>2</sub>,  $t_{\text{ox}}$  is the thickness of SiO<sub>2</sub>, and  $\epsilon_0$  is the vacuum permittivity. As shown in Figure S16, the charge neutral point (CNP) was observed to be at 2 V so that the n-type carrier concentration could be estimated by using Eq. (2), which yielded  $-7.19 \times 10^{11} \text{ cm}^{-2}$ ,  $-4.31 \times 10^{12} \text{ cm}^{-2}$ , and  $-7.91 \times 10^{12} \text{ cm}^{-2}$  for 0 V, -10 V and -20 V, respectively. Given a carrier concentration  $n$ , the corresponding Fermi-level position could be estimated by using the following expression for semiconductors:

$$E_f - E_c = k_B T \ln(e^{n/g_{2D}k_B T} - 1), \quad (3)$$

where  $E_f$  is the Fermi-level energy,  $E_c$  is the conduction band edge,  $g_{2D} = g_v m^* / \pi \hbar^2$  is the density of the states,  $g_v$  is the valley degeneracy factor, and  $m^* = 0.34 m_0$ . Therefore, the Fermi-level position was estimated to be 0.3 eV, 0.25 eV and 0.23 eV lower than the conduction band minimum for 0 V, -10 V and -20 V, respectively. As shown in Figures 5d–5f, the degree of valley polarization steadily increased with the carrier density at RT, which may be attributed to the noticeable screening effect by the doped carriers.

Specifically, the mechanism for the enhancement of valley polarization by electrostatic doping in the WS<sub>2</sub>-2TRHPAS heterostructure may be attributed to carrier doping-induced suppression on the inter-valley relaxation process. The inter-valley relaxation process of bright excitons is dominated by the long range electron-hole (e-h) exchange interaction, and the long-range e-h exchange interactions can be efficiently screened by adding 2D electrons/holes with electrostatic doping.<sup>[55]</sup> The screen length is determined by the inverse of the Thomas-Fermi wave vector, which is given by the following expression:<sup>[55]</sup>

$$k_{TF}(T, E_f) = k_{TF0} \left[ 1 - e^{-(E_f/k_B T)} \right], \quad (4)$$

where  $k_{TF0} = g_s g_v m^* e^2 / (4\pi \epsilon \hbar^2)$  is the zero temperature Thomas-Fermi wave vector,  $g_s$  ( $g_v$ ) is the degeneracy for spins (valleys),  $m^*$  is the effective electron or hole mass, and  $\epsilon$  is the dielectric constant. The Fermi energy  $E_f$  measured from the bottom of the conduction band (to the top of the valance band) is defined by  $E_f = 2\pi n \hbar^2 / (g_s g_v m^*)$ , where  $n$  is the doped electron (hole) density. Therefore,  $k_{TF}$  increases rapidly with increasing  $n$  according to Eq. (4). In the strong scattering limit, the inter-valley scattering rate  $(\tau_v)^{-1}$  due to e-h exchange interaction may be approximated by the relation  $(\tau_v)^{-1} \propto (k_{TF})^{-2}$ .<sup>[55]</sup> Therefore, the inter-valley scattering rate  $(\tau_v)^{-1}$  is strongly suppressed by carrier doping. In contrast, the intra-valley relaxation time  $\tau_0$  is much less affected by carrier doping, as supported by the stable linewidths and integrated intensities upon doping.<sup>[56]</sup> Our

work aims to tailor the degree of valley polarization by manipulating the inter-valley scattering rate  $(\tau_v)^{-1}$  via tuning the carrier doping. Noting that the valley polarization  $P_{DVP}$ <sup>[57]</sup> is given by

$$P_{DVP} = \frac{P_0}{1+2(\tau_0/\tau_v)}, \quad (5)$$

where  $P_0$  is the ideal valley polarization, we find that the suppression of  $(\tau_v)^{-1}$  by electrostatic doping leads to the enhancement of  $P_{DVP}$ , which agrees well with our experimental observations.

### Conclusion

In summary, we have demonstrated that ultra-compact plasmonic Archimedes spiral (PAS) nanostructures can efficiently tailor the valley-polarized PL of monolayer  $WS_2$  at room temperature. The chiral-SPP focusing fields from the PAS nanostructures can significantly amplify the exciton/trion emissions in the  $WS_2$  monolayer with specific chiral emission due to the interaction of  $WS_2$  excitons/trions with the plasmons of the PAS nanostructures. The plasmon-exciton coupling is shown to provide control of the valley-polarized PL through manipulating the imbalance of valley population, leading to significant PL modulations through valley-dependent control of the excitonic emissions at room temperature. In particular, we have demonstrated enhancement of the degrees of valley polarization (DVP) at room temperature from  $\sim 3\%$  for the as-grown 1L- $WS_2$  to  $\sim 40\%$  for the 1L- $WS_2$ -2TRHPAS heterostructures and to  $\sim 50\%$  for the 1L- $WS_2$ -4T RHPAS heterostructures. Furthermore, by applying a back-gate bias voltage ( $V_{Gate}$ ), the valley polarization is found to be further enhanced from 40% to 70% for  $V_{Gate} = -20$  V, which implies that the excess carrier doping can enhance the valley polarization by screening of the momentum-dependent long-range electron-hole exchange interaction and therefore reducing the inter-valley scattering. The methodology described in this work provides a promising platform to manipulate the valley degrees of freedom in 2H-TMDs efficiently at room temperature, paving ways for future applications of opto-valleytronic/spintronic devices based on these 2D materials.

## Experimental Section

*Synthesis of WS<sub>2</sub>*: Monolayer WS<sub>2</sub> was grown by using APCVD as reported previously. 95 mg WO<sub>3</sub> precursor mixed with 5 mg KI was placed in a quartz boat containing the SiO<sub>2</sub>/Si substrates that were set face-down directly above the W source precursor, and the quartz boat was then positioned at the center of the furnace. A second boat containing 100 mg S was placed upstream at 18 cm away from the W source. Next, the system was pump down to  $3 \times 10^{-2}$  torr to eliminate air and moisture. After the system reached the base pressure, the Ar/H<sub>2</sub> (80/40 sccm) carrier gas was introduced until atmospheric pressure was achieved. The furnace was then heated up with a ramp rate of 35 °C/min to the growth temperatures (750 to 850 °C). The S component melted at 150 °C was sent into the furnace at the growth temperature to grow WS<sub>2</sub>. The sample growth procedure proceeded for 10 minutes, after which the furnace was directly opened to room temperature to stop the reaction immediately.

*Transfer of mono- and multi-layer WS<sub>2</sub>*: Polystyrene (PS) was used as the supplementary film to peel off the WS<sub>2</sub> crystals from sapphire substrates. PS (M.W. 192000) dispersed in toluene solution (20 mg/mL) was spin-coated on top of the WS<sub>2</sub> sample at a speed of 3000 rpm. The edge of the PS film was scribed with a blade, and then the sample of PS/WS<sub>2</sub>/Si-substrate was inserted into water slowly. The PS/WS<sub>2</sub> film became peeled off naturally in water, and was subsequently rinsed with deionized-water thrice before it was picked up and placed onto the target substrate. The PS coating was removed with toluene after baking the sample at 80 °C for 60 minutes.

*PL and TRPL Characterizations*: The PL spectra were taken with a Renishaw InVia Raman spectrometer system using a 514.3 nm laser (2.41 eV) as the excitation source. A 50× objective lens with a numerical aperture of 0.75 and a 2400 lines/mm and 1800 lines/mm grating were chosen during the measurement to achieve better signal-to-noise ratio. The time-resolved PL measurements

This article is protected by copyright. All rights reserved.

were taken on an inverted microscope (Zeiss Axio Observer) equipped with an avalanche photodiode (Picoquant PDM series with PicoHarp 300 timing electronics). For the PL lifetime measurements, a 532 nm picosecond laser diode (70 ps pulse duration, 40 MHz repetition rate; PicoQuant) excitation source was used, and a 532 nm band pass filter was placed after laser source to purify the laser beam. A 100× objective lens with a numerical aperture of 0.9 (Zeiss, Inc.) was used to focus the pulsed laser to a small spot of  $1.6 \times 10^{-6} \text{ cm}^2$  with an estimated peak power density of  $7.5 \text{ kW cm}^{-2}$ .

*Device Preparation and Device Measurements:* The MDMs were fabricated on a heavily p-doped Si substrate via an E-beam evaporator and PECVD. The 150 nm-thick gold mirror layer was deposited on the heavily p-doped Si substrate by E-beam evaporation. Then, a thin silicon oxide (~10 nm) layer was deposited by PECVD. After forming 10 nm SiO<sub>2</sub> layer on top of the Au/Si substrate, an annealing treatment in Ar at 1050 °C for 5 hours was followed by the growth of an additional oxide to the final thickness (60 nm). The CVD-grown WS<sub>2</sub> was transferred on to the dielectric spacer using the method described above. Lastly, the Archimedes spiral rings were patterned by E-beam lithography on a 50 nm-thick Au film deposited on the WS<sub>2</sub>-PAS. The electrical properties of the WS<sub>2</sub>-2TRHPAS FETs were studied using a Keithley 2636 sourcemeter as a DC voltage source in vacuum at 300 K.

### Supporting Information

Supporting Information is available from the Wiley Online Library or from the author.

**Acknowledgements**

This work was jointly supported by the Army Research Office under the Multi-University Research Initiative (MURI) program (award #W911NF-16-1-0472) and the National Science Foundation under the Physics Frontier Center program for Institute for Quantum Information and Matter (IQIM) at the California Institute of Technology (award #1733907). The authors are also grateful for the support from the Beckman Institute at the California Institute of Technology for access to facilities at the Molecular Materials Research Center. W-H Lin acknowledges a graduate fellowship from the J. Yang Family Foundation. P.C.W. acknowledges the support from the Ministry of Science and Technology (MOST), Taiwan (Grant number: 107-2923-M-006-004-MY3; 108-2112-M-006-021-MY3; 110-2124-M-006-004), and in part from the Higher Education Sprout Project of the Ministry of Education (MOE) to the Headquarters of University Advancement at National Cheng Kung University (NCKU). P.C.W. also acknowledges the support from the Ministry of Education (Yushan Young Scholar Program). The authors also thank Wen-Hui Cheng for training on atomic layer deposition (ALD) system.

**Conflict of Interest**

The authors declare no conflict of interest.

**Keywords**

transition metal dichalcogenides, exciton-plasmon interaction, valleytronics, circular dichroism, chiral plasmonic metasurface

Received: ((will be filled in by the editorial staff))

Revised: ((will be filled in by the editorial staff))

Published online: ((will be filled in by the editorial staff))

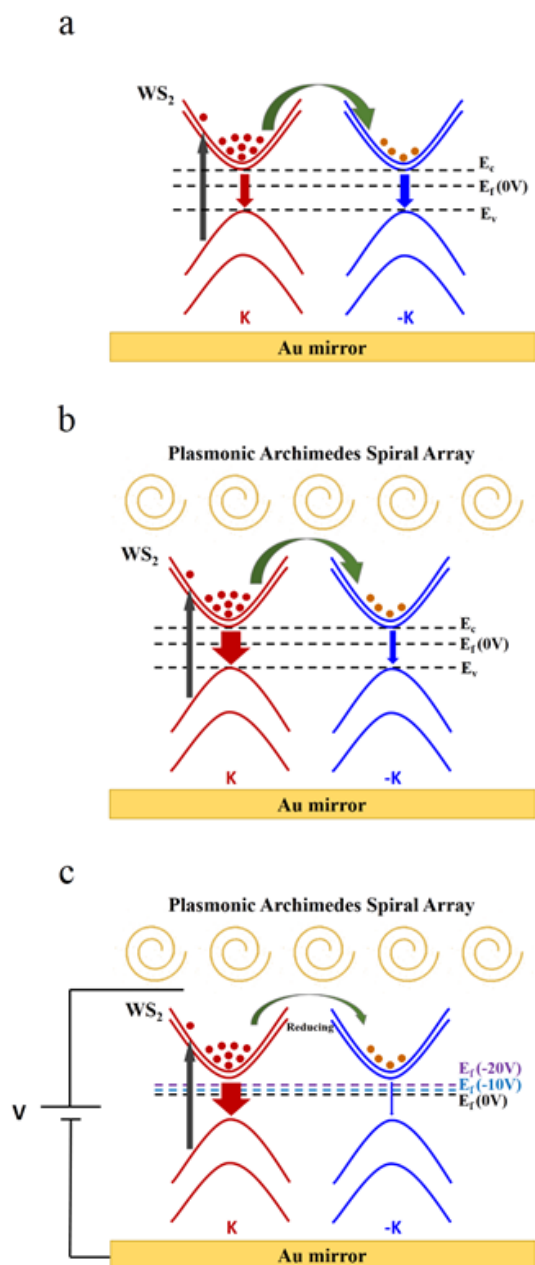


**Figure 1.** Proposed mechanism for tailoring the valley-polarized PL of gated WS<sub>2</sub>-RHPAS heterostructure: a) Schematics of the energy bands of monolayer WS<sub>2</sub> under right-handed CPL with significant inter-valley scattering. b) Schematics of the energy bands of monolayer WS<sub>2</sub>-RHPAS heterostructure under right-handed CPL, showing significantly increased decay rate of  $\sigma^+$  excitons. c) Schematics of the energy bands of a gated monolayer WS<sub>2</sub>-RHPAS heterostructure, showing both increased decay rate of  $\sigma^+$  excitons and suppressed inter-valley scattering due to carrier doping-induced screening of the long-range electron-hole interaction.

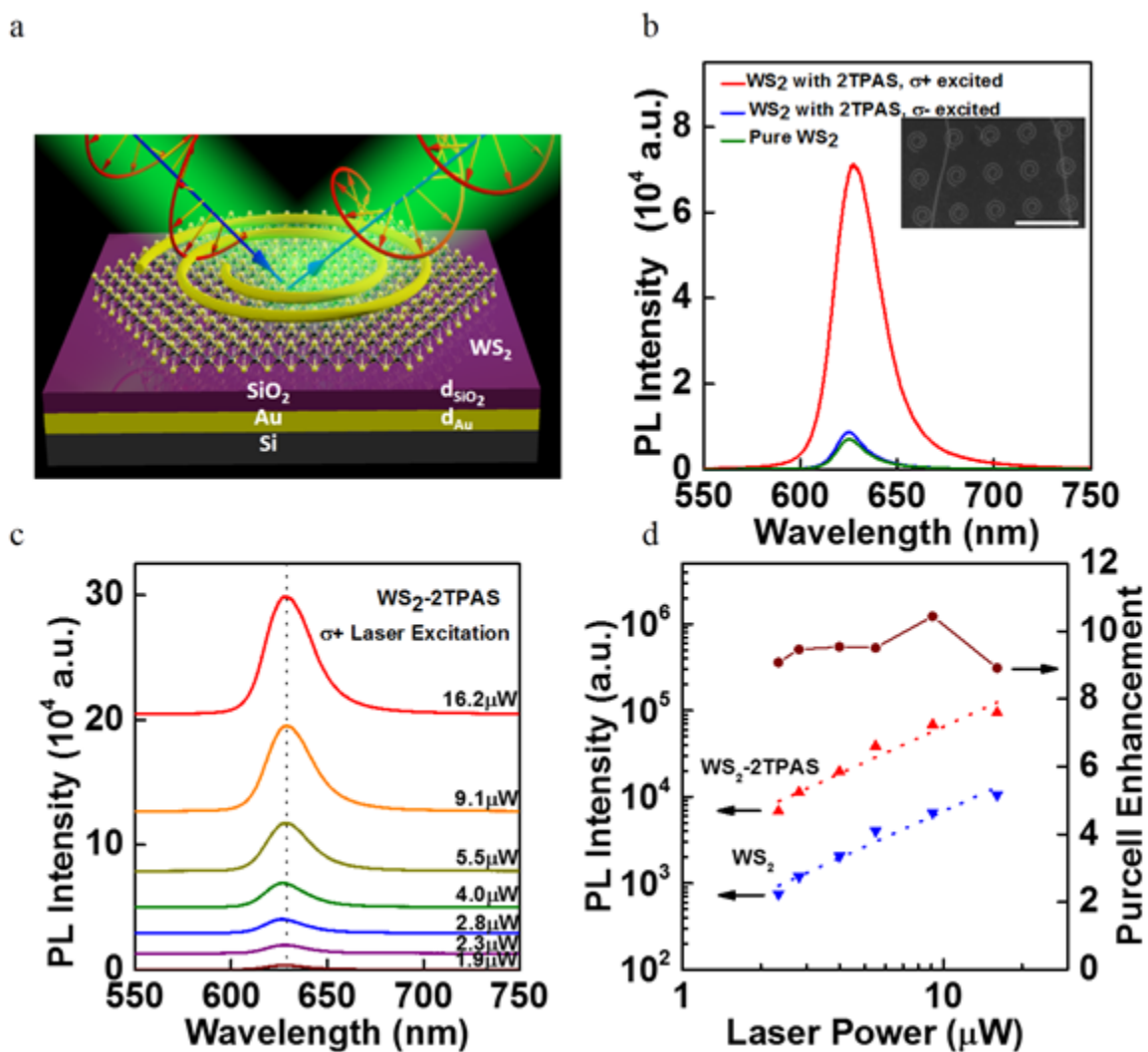


**Figure 2.** Structure and optical spectral properties of monolayer WS<sub>2</sub> integrated with two turns (2T) of right-handed plasmonic Archimedes spiral (WS<sub>2</sub>-2TRHPAS) heterostructures, where the resonance wavelength of PAS ( $R_{\text{plasmon}}$ ) is 620 nm. a) Schematics of a WS<sub>2</sub>-2TRHPAS heterostructure under circular polarized (CP) light excitations, where a CVD-grown monolayer WS<sub>2</sub> is placed on top of a SiO<sub>2</sub> layer sandwiched between Au spiral structures and a Au film. b) PL spectra of monolayer WS<sub>2</sub> with and without the Au spiral structures, under the excitation of different circularly polarized light at 514 nm and the laser power at 8.8  $\mu\text{W}$ . The inset shows an SEM image of the WS<sub>2</sub>-2TRHPAS array and the scale bar is 5  $\mu\text{m}$ . c) Evolution of the PL spectra of monolayer WS<sub>2</sub>-2TRHPAS with laser power. d) Power-dependent PL intensity with (red) and without (blue) Au spiral nanostructures and the corresponding Purcell enhancement (dark red).

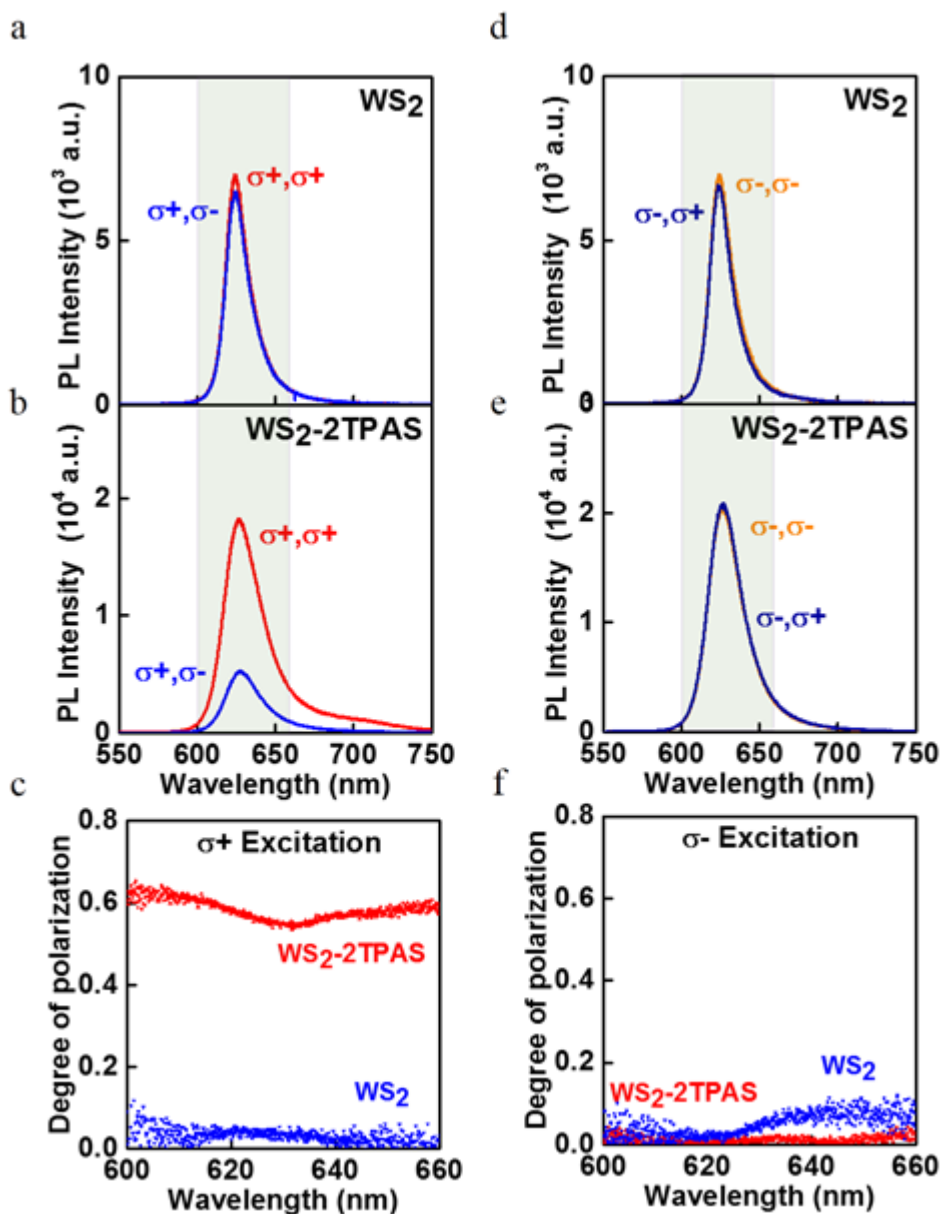


**Figure 3.** Valley-polarized PL spectra of the as-grown WS<sub>2</sub> and WS<sub>2</sub>-2TRHPAS. a) - b) Circularly polarized PL spectra of WS<sub>2</sub> and WS<sub>2</sub>-2TRHPAS under the excitation of  $\sigma^+$  light (514 nm) at RT. d) - e) Circularly polarized PL spectra of WS<sub>2</sub> and WS<sub>2</sub>-2TRHPAS under the excitation of  $\sigma^-$  light (514 nm) at RT. The degrees of valley polarization (DVP) spectra associated with WS<sub>2</sub> and WS<sub>2</sub>-2TRHPAS are shown in c) for  $\sigma^+$  excitations and in f) for  $\sigma^-$  excitations.

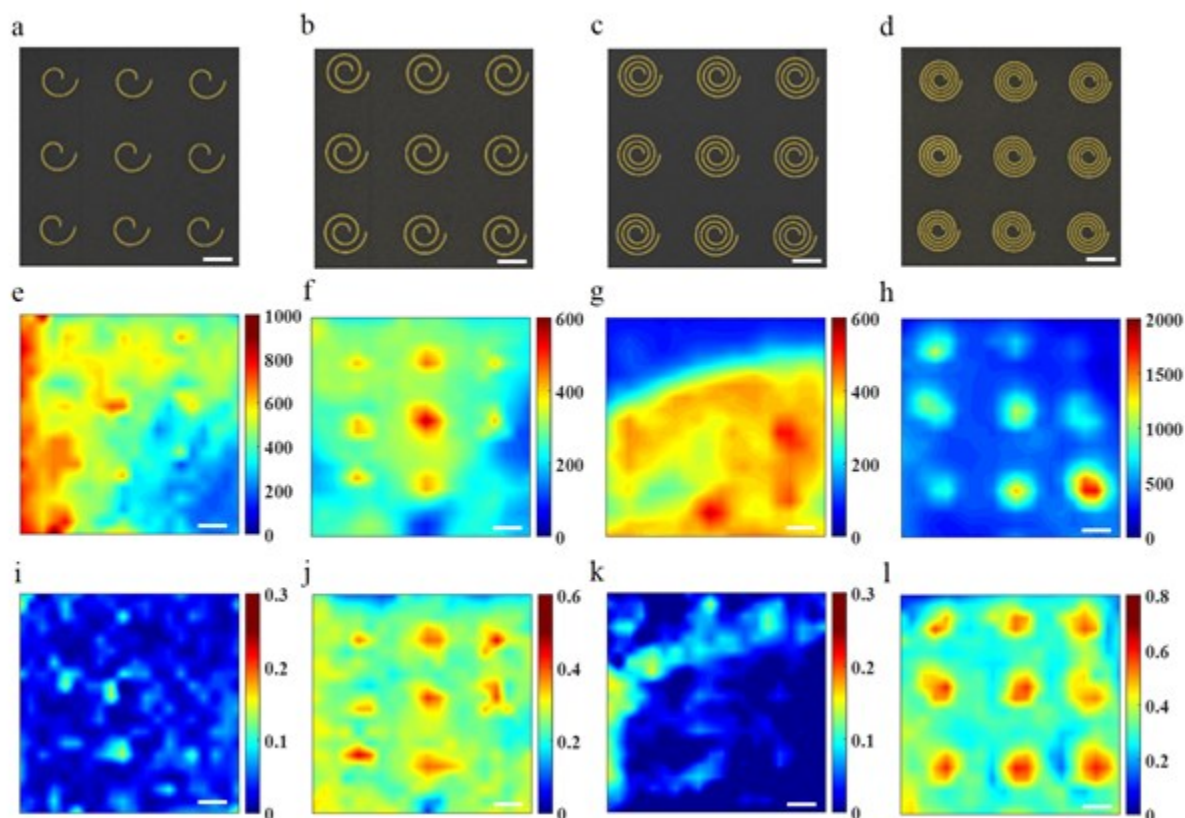


**Figure 4.** Dependence of the RT valley polarization of  $WS_2$ -RHPAS structures on the ring number of PAS: a-d) SEM images of 1-, 2-, 3- and 4-turn RHPAS arrays. (Scale bar:  $1.25 \mu\text{m}$ ). e-h) PL intensity mapping of  $WS_2$  samples with 1-, 2-, 3- and 4-turn RHPAS arrays under  $\sigma^+$  (RCP) excitation at 514 nm. Apparent focusing effects can be obtained from 2- and 4-turn RHPAS arrays, in contrast to the absence of focusing effects from 1- and 3-turn RHPAS arrays. (Scale bar:  $1.25 \mu\text{m}$ ). i-l) Maps of the degrees of valley polarization (DVP) taken on  $WS_2$  with 1-, 2-, 3- and 4-turn RHPAS arrays under the RCP excitation. Apparently high values of DVP can be obtained at RT from  $WS_2$  with 2- and 4-turn RHPAS arrays (Scale bar:  $1.25 \mu\text{m}$ ).

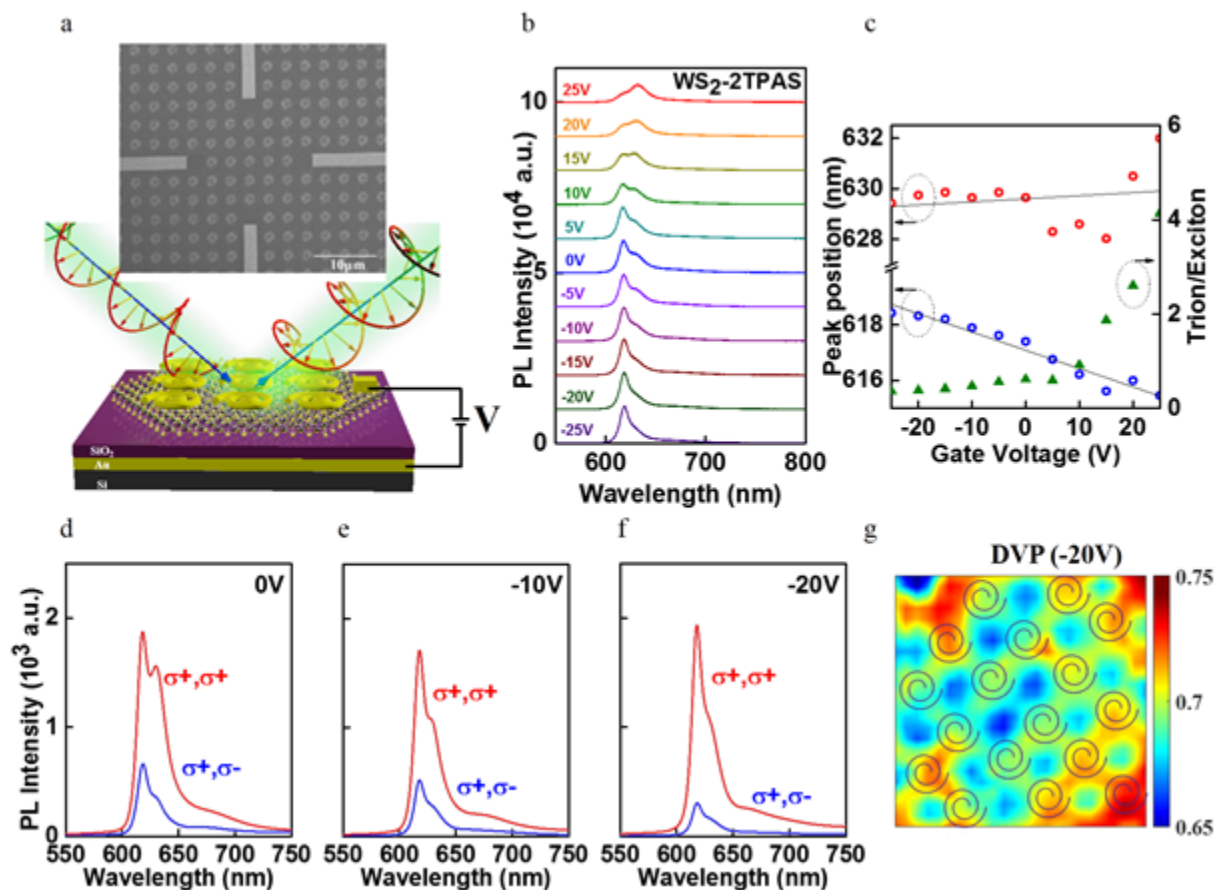


**Figure 5.** a) Electrically tunable valley polarization of WS<sub>2</sub>-2TRHPAS heterostructure. b) PL spectra at RT for  $V_{\text{Gate}}$  from  $-25$  V to  $25$  V, with an increment of  $5$  V. c) Gate voltage dependence of the PL peak position for neutral excitons (blue) and trions (red) under  $V_{\text{Gate}}$  from  $-25$  V to  $25$  V. The intensity ratio of trions and excitons (green) is also shown as a function of  $V_{\text{Gate}}$  from  $-25$  V to  $25$  V. The  $\sigma^+$  (red) and  $\sigma^-$  (blue) PL intensity taken at RT under d)  $V_{\text{Gate}} = 0$ , e)  $V_{\text{Gate}} = -10$  V, and f)  $V_{\text{Gate}} = -20$  V, respectively. g) Spatial map of the DVP in a WS<sub>2</sub>-2TRHPAS heterostructure under  $V_{\text{Gate}} = -20$  V at RT.

## References

- [1] K. F. Mak, C. Lee, J. Hone, J. Shan, T. F. Heinz, *Phys. Rev. Lett.* **2010**, *105*, 136805.
- [2] A. Splendiani, L. Sun, Y. Zhang, T. Li, J. Kim, C.-Y. Chim, G. Galli, F. Wang, *Nano Lett.* **2010**, *10*, 1271.
- [3] S. Z. Butler, S. M. Hollen, L. Cao, Y. Cui, J. A. Gupta, H. R. Gutiérrez, T. F. Heinz, S. S. Hong, J. Huang, A. F. Ismach, E. Johnston-Halperin, M. Kuno, V. V. Plashnitsa, R. D. Robinson, R. S. Ruoff, S. Salahuddin, J. Shan, L. Shi, M. G. Spencer, M. Terrones, W. Windl, J. E. Goldberger, *ACS Nano* **2013**, *7*, 2898.
- [4] R. Ganatra, Q. Zhang, *ACS Nano* **2014**, *8*, 4074.
- [5] J.-K. Huang, J. Pu, C.-L. Hsu, M.-H. Chiu, Z.-Y. Juang, Y.-H. Chang, W.-H. Chang, Y. Iwasa, T. Takenobu, L.-J. Li, *ACS Nano* **2014**, *8*, 923.
- [6] Q. H. Wang, K. Kalantar-Zadeh, A. Kis, J. N. Coleman, M. S. Strano, *Nature Nanotechnology* **2012**, *7*, 699.
- [7] F. Xia, H. Wang, D. Xiao, M. Dubey, A. Ramasubramaniam, *Nature Photonics* **2014**, *8*, 899.
- [8] H. Zeng, J. Dai, W. Yao, D. Xiao, X. Cui, *Nature Nanotechnology* **2012**, *7*, 490.
- [9] K. F. Mak, K. He, J. Shan, T. F. Heinz, *Nature Nanotechnology* **2012**, *7*, 494.
- [10] T. Cao, G. Wang, W. Han, H. Ye, C. Zhu, J. Shi, Q. Niu, P. Tan, E. Wang, B. Liu, J. Feng, *Nature Communications* **2012**, *3*, 887.
- [11] D. Xiao, G.-B. Liu, W. Feng, X. Xu, W. Yao, *Phys. Rev. Lett.* **2012**, *108*, 196802.
- [12] G. Wang, A. Chernikov, M. M. Glazov, T. F. Heinz, X. Marie, T. Amand, B. Urbaszek, *Rev. Mod. Phys.* **2018**, *90*, 021001.
- [13] W.-H. Lin, W.-S. Tseng, C. M. Went, M. L. Teague, George. R. Rossman, H. A. Atwater, N.-C. Yeh, *ACS Nano* **2020**, *14*, 1350.
- [14] D. Xiao, W. Yao, Q. Niu, *Phys. Rev. Lett.* **2007**, *99*, 236809.
- [15] W. Yao, D. Xiao, Q. Niu, *Phys. Rev. B* **2008**, *77*, 235406.
- [16] J. S. Ross, S. Wu, H. Yu, N. J. Ghimire, A. M. Jones, G. Aivazian, J. Yan, D. G. Mandrus, D. Xiao, W. Yao, X. Xu, *Nature Communications* **2013**, *4*, 1474.
- [17] M. Schadt, *Annu. Rev. Mater. Sci.* **1997**, *27*, 305.
- [18] L. Albani, C. Marchessoux, T. Kimpe, *Information Display* **2011**, *27*, 24.

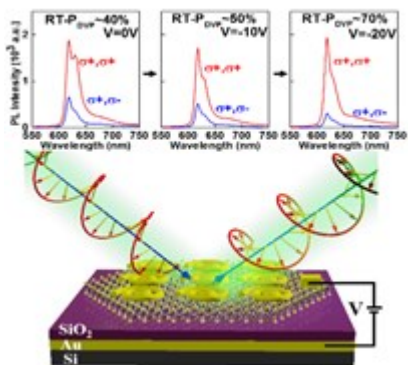
- [19] R. Farshchi, M. Ramsteiner, J. Herfort, A. Tahraoui, H. T. Grahn, *Appl. Phys. Lett.* **2011**, *98*, 162508.
- [20] K. Hammerer, A. S. Sørensen, E. S. Polzik, *Rev. Mod. Phys.* **2010**, *82*, 1041.
- [21] R. Ursin, T. Jennewein, M. Aspelmeyer, R. Kaltenbaek, M. Lindenthal, P. Walther, A. Zeilinger, *Nature* **2004**, *430*, 849.
- [22] G. Wang, E. Palleau, T. Amand, S. Tongay, X. Marie, B. Urbaszek, *Appl. Phys. Lett.* **2015**, *106*, 112101.
- [23] W. Yang, J. Shang, J. Wang, X. Shen, B. Cao, N. Peimyoo, C. Zou, Y. Chen, Y. Wang, C. Cong, W. Huang, T. Yu, *Nano Lett.* **2016**, *16*, 1560.
- [24] A. M. Jones, H. Yu, N. J. Ghimire, S. Wu, G. Aivazian, J. S. Ross, B. Zhao, J. Yan, D. G. Mandrus, D. Xiao, W. Yao, X. Xu, *Nature Nanotechnology* **2013**, *8*, 634.
- [25] Z. Wang, Z. Dong, Y. Gu, Y.-H. Chang, L. Zhang, L.-J. Li, W. Zhao, G. Eda, W. Zhang, G. Grinblat, S. A. Maier, J. K. W. Yang, C.-W. Qiu, A. T. S. Wee, *Nature Communications* **2016**, *7*, 11283.
- [26] Y. You, X.-X. Zhang, T. C. Berkelbach, M. S. Hybertsen, D. R. Reichman, T. F. Heinz, *Nature Physics* **2015**, *11*, 477.
- [27] W.-T. Hsu, Y.-L. Chen, C.-H. Chen, P.-S. Liu, T.-H. Hou, L.-J. Li, W.-H. Chang, *Nature Communications* **2015**, *6*, 8963.
- [28] S. Wu, J. S. Ross, G.-B. Liu, G. Aivazian, A. Jones, Z. Fei, W. Zhu, D. Xiao, W. Yao, D. Cobden, X. Xu, *Nature Physics* **2013**, *9*, 149.
- [29] G. Aivazian, Z. Gong, A. M. Jones, R.-L. Chu, J. Yan, D. G. Mandrus, C. Zhang, D. Cobden, W. Yao, X. Xu, *Nature Physics* **2015**, *11*, 148.
- [30] Y. Li, J. Ludwig, T. Low, A. Chernikov, X. Cui, G. Arefe, Y. D. Kim, A. M. van der Zande, A. Rigosi, H. M. Hill, S. H. Kim, J. Hone, Z. Li, D. Smirnov, T. F. Heinz, *Phys. Rev. Lett.* **2014**, *113*, 266804.
- [31] D. MacNeill, C. Heikes, K. F. Mak, Z. Anderson, A. Kormányos, V. Zólyomi, J. Park, D. C. Ralph, *Phys. Rev. Lett.* **2015**, *114*, 037401.
- [32] K. F. Mak, J. Shan, *Nature Photonics* **2016**, *10*, 216.
- [33] A. Srivastava, M. Sidler, A. V. Allain, D. S. Lembke, A. Kis, A. Imamoglu, *Nature Physics* **2015**, *11*, 141.
- [34] H.-T. Lin, C.-Y. Chang, P.-J. Cheng, M.-Y. Li, C.-C. Cheng, S.-W. Chang, L. L. J. Li, C.-W. Chu, P.-K. Wei, M.-H. Shih, *ACS Appl. Mater. Interfaces* **2018**, *10*, 15996.
- [35] T. Wen, W. Zhang, S. Liu, A. Hu, J. Zhao, Y. Ye, Y. Chen, C.-W. Qiu, Q. Gong, G. Lu, *Science Advances* **2020**, *6*, eaao0019.

- [36] Q. Jiang, B. Du, M. Jiang, D. Liu, Z. Liu, B. Li, Z. Liu, F. Lin, X. Zhu, Z. Fang, *Nanoscale* **2020**, *12*, 5906.
- [37] J. Sun, H. Hu, D. Pan, S. Zhang, H. Xu, *Nano Lett.* **2020**, *20*, 4953.
- [38] K. Shinokita, X. Wang, Y. Miyauchi, K. Watanabe, T. Taniguchi, K. Matsuda, *Advanced Functional Materials* **2019**, *29*, 1900260.
- [39] Z. Li, Y. Li, T. Han, X. Wang, Y. Yu, B. Tay, Z. Liu, Z. Fang, *ACS Nano* **2017**, *11*, 1165.
- [40] Z. Li, C. Liu, X. Rong, Y. Luo, H. Cheng, L. Zheng, F. Lin, B. Shen, Y. Gong, S. Zhang, Z. Fang, *Advanced Materials* **2018**, *30*, 1801908.
- [41] Z. Wu, J. Li, X. Zhang, J. M. Redwing, Y. Zheng, *Advanced Materials* **2019**, *31*, 1904132.
- [42] M. Deng, X. Wang, J. Chen, Z. Li, M. Xue, Z. Zhou, F. Lin, X. Zhu, Z. Fang, *Advanced Functional Materials* **2021**, *31*, 2010234.
- [43] L. Zheng, Z. Liu, D. Liu, X. Wang, Y. Li, M. Jiang, F. Lin, H. Zhang, B. Shen, X. Zhu, Y. Gong, Z. Fang, *Nat Commun* **2021**, *12*, 291.
- [44] V. K. Valev, N. Smisdom, A. V. Silhanek, B. De Clercq, W. Gillijns, M. Ameloot, V. V. Moshchalkov, T. Verbiest, *Nano Lett.* **2009**, *9*, 3945.
- [45] M. Kuwata-Gonokami, N. Saito, Y. Ino, M. Kauranen, K. Jefimovs, T. Vallius, J. Turunen, Y. Svirko, *Phys. Rev. Lett.* **2005**, *95*, 227401.
- [46] M. J. Huttunen, G. Bautista, M. Decker, S. Linden, M. Wegener, M. Kauranen, *Opt. Mater. Express, OME* **2011**, *1*, 46.
- [47] M. Decker, R. Zhao, C. M. Soukoulis, S. Linden, M. Wegener, *Opt. Lett., OL* **2010**, *35*, 1593.
- [48] E. Plum, X.-X. Liu, V. A. Fedotov, Y. Chen, D. P. Tsai, N. I. Zheludev, *Phys. Rev. Lett.* **2009**, *102*, 113902.
- [49] C. Zhang, K. Wu, V. Giannini, X. Li, *ACS Nano* **2017**, *11*, 1719.
- [50] A. Belardini, M. C. Larciprete, M. Centini, E. Fazio, C. Sibilia, D. Chiappe, C. Martella, A. Toma, M. Giordano, F. Buatier de Mongeot, *Phys. Rev. Lett.* **2011**, *107*, 257401.
- [51] N. Meinzer, E. Hendry, W. L. Barnes, *Phys. Rev. B* **2013**, *88*, 041407.
- [52] M. Cotrufo, C. I. Osorio, A. F. Koenderink, *ACS Nano* **2016**, *10*, 3389.
- [53] V. K. Valev, J. J. Baumberg, C. Sibilia, T. Verbiest, *Advanced Materials* **2013**, *25*, 2517.
- [54] S. Kühn, U. Håkanson, L. Rogobete, V. Sandoghdar, *Phys. Rev. Lett.* **2006**, *97*, 017402.
- [55] S. Konabe, *Appl. Phys. Lett.* **2016**, *109*, 073104.
- [56] S. Mouri, Y. Miyauchi, K. Matsuda, *Nano Lett.* **2013**, *13*, 5944.

This article is protected by copyright. All rights reserved.

[57] S. Feng, C. X. Cong, S. Konabe, J. Zhang, J. Z. Shang, Y. Chen, C. J. Zou, B. C. Cao, L. S. Wu, N. Peimyoo, B. L. Zhang, T. Yu, *Small* **2019**, 15, 1805503.

TOC



Efficient tailoring of valley-polarized photoluminescence from monolayer  $\text{WS}_2$  at room temperature (RT) through surface plasmon-exciton interactions with plasmonic Archimedes spiral (PAS) nanostructures is achieved in this manuscript. The degree of valley polarization of  $\text{WS}_2$ -PAS heterostructures at RT can be enhanced from 40% to 70% by modulating the carrier doping via a backgate field effect transistor (FET) device.